Contents lists available at ScienceDirect

Environmental Toxicology and Pharmacology

The use of a complex tetra-culture alveolar model to study the biological effects induced by gold nanoparticles with different physicochemical properties

Melissa Saibene [a,b], Tommaso Serchi [a], Patrizia Bonfanti [b], Anita Colombo [b], Inge Nelissen [c], Rashi Halder [e], Jean-Nicolas Audinot [f], Beatriz Pelaz [g,h], Mahmoud G. Soliman [d,i,j], Wolfgang J. Parak [d,k], Paride Mantecca [b], Arno C. Gutleb [a], Sebastien Cambier [a,*]

[a] EH Group, SUSTAIN Unit, ERIN Department, Luxembourg Institute of Science and Technology, Luxembourg
[b] Polaris Research Centre, DISAT, University of Milano-Bicocca, Italy
[c] Health Unit, Flemish Institute for Technological Research (VITO nv), Mol, Belgium
[d] Center for Hybrid Nanostructures, University of Hamburg, Germany
[e] Sequencing platform, LCSB, University of Luxembourg, Luxembourg
[f] AINA Group, SIPT Unit, MRT Department, Luxembourg Institute of Science and Technology, Luxembourg
[g] Centro Singular de Investigación en Química Biolóxica e Materiais Moleculares (CiQUS), Universidade de Santiago de Compostela, Spain
[h] Departamento de Química Inorgánica, Grupo de Física de Coloides y Polímeros, Universidade de Santiago de Compostela, Spain
[i] Chemistry Department, RCSI, Ireland
[j] Physics Department, Faculty of Science, Al-Azhar University, Egypt
[k] The Hamburg Centre for Ultrafast Imaging, Germany

ARTICLE INFO

ABSTRACT

A substantial increase in engineered nanoparticles in consumer products has been observed, heightening human and environmental exposure. Inhalation represents the primary route of human exposure, necessitating a focus on lung toxicity studies. However, to avoid ethical concerns the use of *in vitro* models is an efficient alternative to *in vivo* models. This study utilized an *in vitro* human alveolar barrier model at air-liquid-interface with four cell lines, for evaluating the biological effects of different gold nanoparticles. Exposure to PEGylated gold nanospheres, nanorods, and nanostars did not significantly impact viability after 24 h, yet all AuNPs induced cytotoxicity in the form of membrane integrity impairment. Gold quantification revealed cellular uptake and transport. Transcriptomic analysis identified gene expression changes, particularly related to the enhancement of immune cells. Despite limited impact, distinct effects were observed, emphasizing the influence of nanoparticles physicochemical parameters while demonstrating the model's efficacy in investigating particle biological effects.

1. Introduction

In the field of human exposure, not all the possible exposure routes are considered to be equally relevant for human toxicity. It is well-established that nanomaterials (NMs) are not able to cross the intact epidermis and that the uptake following ingestion is very little and limited to specific NMs of small size only (e.g. TiO2, (Lamas et al., 2020)). On the contrary, the inhalation route is considered to be extremely relevant for NMs and for this reason, lung toxicity studies should be considered a priority. The scientific challenge is to relate measurements of particle size, number and mass concentrations, human exposure, inhaled and internal dose, synergistic processes and, finally, potential adverse health effects.

Depending on particle dimensions, different airways tracts are

affected. NPs can deposit throughout the entire respiratory tract with the ability to ultimately reach the alveoli, the terminal part of the airways (Lazaridis, 2023; Oberdörster et al., 2005). The alveoli constitute the largest lung area and the interalveolar septum acts as the main barrier between the environment and the systemic circulation. Upon interaction with the air-blood-barrier, NPs may be able to cross the alveolar barrier and reach the systemic circulation, especially when they are between 100 nm and 10 nm (Braakhuis et al., 2015). Once in the systemic circulation, NPs can reach other tissues, cause damage, and accumulate in secondary target organs such as the heart, pancreas, liver, kidney and spleen (Yacobi et al., 2011).

Since the use of animals, mainly rodents, in toxicological practices poses ethical and social concerns (Russell and Burch, 1959) and is not aligned with the 3 R principles, the development of new approach methodologies in inhaled particulate matter health assessment is of paramount importance in term toxicant-target interactions, fate and biological response (Lazaridis, 2023). The use of complex *in vitro* lung models offers a relevant alternative to *in vivo* studies for predicting the acute toxicity of inhaled substances (such as gases, volatile organic compounds, PAH and particulate matter including nanoparticles) (Müller et al., 2011; de Souza Carvalho et al., 2014a,b; Jaber and Billet, 2023). However, their suitability for representing the different part of the respiratory system, which comprises around forty different cell types is not widely accepted. The development of relevant *in vitro* models to reflect the effects of chemicals on human tissue requires suitable culture conditions in terms of the air-liquid-interface (ALI) and use of co-cultures/3D models (Silva et al., 2023). Several studies reporting *in vivo* and *in vitro* exposure to different NPs Ag, ZnO, TiO_2 and multi-walled carbon nanotubes were compared and after exposure to aerosolized NP suspensions, responses were similar in terms of cytotoxicity and inflammation under *in vitro* and *in vivo* conditions (Secondo et al., 2017).

In recent years, several *in vitro* lung models have been proposed for inhalation toxicity studies, including some commercial models that are available on the market (i.g.: Mucilair®). These *in vitro* models include systems ranging from a simple monoculture (2D culture) in submerged conditions to complex co-culture in 3D orientation. These models have different levels of complexity in order to mimic tissue organization and to simulate the response of the human lung tissue (Rothen-Rutishauser et al., 2005; Blank et al., 2006; Kim and Ryu, 2013; Klein et al., 2013; Schürch et al., 2014; Braakhuis et al., 2016; Chary et al., 2019; Marescotti et al., 2019). In parallel, advances have been made to develop models that allow the exposure of the cells at the ALI to be closer to the *in vivo* scenario.

The model used in this work is composed of four different human lung cell lines developed by Klein et al., 2013. This co-culture resembles the *in vivo* organization of the human lung alveoli; the different cell lines involved are epithelial cells (A549), mast cells (HMC-1) and macrophage-like cells (differentiated THP-1) on the apical side of a transwell insert membrane and endothelial cells (EA.hy926) seeded on the basolateral side of the transwell membrane. It has been demonstrated that the different cell types communicate with each other (Marescotti et al., 2019). When mono-, bi- and tetra-cultures were treated with 20 mM of AAPH (2,2′-azobis-2-methyl-propanimidamide--dihydrochloride), the tetra- and the mono-cultures showed different responses in terms of oxidative stress and interleukin-8 (IL-8) release (Klein et al., 2013).

In addition, when established, a thin layer of surfactant composed of surface-active lipid-protein material was characterized protecting the cells at the ALI (Klein et al., 2013). *In vivo*, the surfactant is composed of 90% lipids and 10% proteins, of which the most abundant and important are Surfactant Protein A, B and C (SP-A; SP-B; SP-C) (Hidalgo et al., 2015). The presence of macromolecules in the surfactant may modify the agglomeration state of NPs, which, in turn, could enhance the phagocytic process exerted by resident macrophages. Therefore, to enable realistic *in vivo*-like exposure, *in vitro* models for inhalation

nanotoxicology should allow for culture of cells at the ALI and the production of surfactant (Lacroix et al., 2018). This co-culture was described as the most physiologically relevant *in vitro* system in comparison to *in vivo* to human lung alveoli (Marescotti et al., 2019). Among NPs, gold NPs (AuNPs) are frequently used, with applications in cosmetic products and in the medical field (Vetten et al., 2013). Due to their acceptable biocompatibility, AuNPs are used in nanomedicine as a potential nanocarrier for active principles (drug delivery), as a nano-sensor, and in photothermal therapy or tracking. Furthermore, anisotropic AuNPs displayed significant changes in their physicochemical properties (Ortiz-Castillo et al., 2020) with a deep and critical perspective in many different fields of use, such as biological and chemical sensing (Falahati et al., 2020), cancer drug delivery (Dreaden et al., 2012), and the regulation of cell function and behavior (Bodelón et al., 2017).

In this study, we investigated the suitability of our in-house developed complex *in vitro* tetra-culture alveolar model (Klein et al., 2013) for assessing the biological fate and effects of different AuNP shapes. We used a set of similar size PEGylated AuNP shape variants (around 60 nm), consisting of gold nanospheres (GNPs), gold nanorods (GNRs) and gold nanostars (GNSs). The cellular model was exposed at the ALI using the VitroCell® Cloud System, which allows aerosols to be generated from AuNPs suspensions. The viability, cytotoxicity, NP uptake and localization, and global gene transcription were evaluated 24 h after exposure.

2. Material and methods

2.1. Reagents

All reagents were purchased from Sigma Chemical (Deisenhofen, Germany). Cell culture media and DPBS were purchased from Invitrogen (the Netherlands) and fetal bovine serum (FBS Superior) was obtained from Biochrom (Berlin, Germany). Transwell inserts – Millicell® Hanging Cell Culture Inserts (surface area of 4.5 cm^2; 1 μm pore size; high pore density PET membranes for 6-well plates) were acquired from Millipore (Merck Chemicals N.V./S.A., Belgium). Curosurf® (80 mg/mL of phospholipid fraction from porcine lung – poractant alfa) was kindly provided by Chiesi Farmaceutici (Parma, Italy).

2.2. NP synthesis and characterization

The set of AuNPs included three different-shaped NPs: gold nano-spheres (GNPs), gold nanorods (GNRs) and gold nanostars (GNSs). Details on the synthesis and basic physicochemical characterization data can be found in previous publications (Hühn et al., 2017; Xu et al., 2018) and in the supplementary material section of the Talamini et al. (2017) study (supplementary material from page S3 to S15; https://pubs.acs.org/doi/full/10.1021/acsnano.7b00497). Additional electron micrograph acquisitions were performed on NP suspensions in MilliQ water and in poractant alfa (1:50 in PBS for 1 h, RT). The electron micrograph acquisitions were performed with the Orion Nanofab Helium Ion Microscope (HIM; Zeiss, Peabody, US) with a 25 keV He^+ beam of 0.3 pA for a matrix of 1024 × 1024 pixels and a counting time of 40μs/pixel (Wirtz et al., 2019).

2.3. Cell culture

The human cell lines A549 (Lieber et al., 1976), THP-1 (Tsuchiya et al., 1980) and EA.hy926 (Suggs et al., 1986) were obtained from the American Type Culture Collection (Manassas, VA, USA). HMC-1 (Butterfield et al., 1988) cells were kindly provided by J.H. Butterfield, Mayo Clinic (Rochester, MN, USA). Cells were grown in T75 flasks and trypsinized twice a week (Klein et al., 2013). Cells were maintained in a humidified atmosphere with 5% CO_2 at 37 °C.

2.4. Tetra-culture model

The tetra-culture was prepared according to (Klein et al., 2013). Cells were cultured using different media and were seeded at specified densities (cells/cm^2) on Millicell® Hanging Cell Culture Inserts (surface area of 4.5 cm^2; 1 μm pore size; high pore density PET membranes for 6-well plates; Millipore) and grown until confluency. Inserts were placed in culture plates (6-well plates; Millipore) with 1.5 mL of medium in the upper compartment and 1.5 mL in the lower compartment. EA.hy926 endothelial cells were seeded on inverted transwell inserts (2.4 × 10^{5}cells/cm^2; Millipore, 1 μm pore size). After cell attachment on the basolateral side of the transwell insert, the plate with the transwell inserts was turned back to its original orientation and A549 cells were seeded inside the transwell (1.2 × 10^5 cells/cm^2). Epithelial and endothelial cells were grown for three days at 37 °C and 5% in a humidified incubator.

On day 3, Human THP-1 cells (human acute monocytic leukemia cell line; (Tsuchiya et al., 1980)) grown in RPMI 1640 media containing 10% (v/v) FBS Superior were differentiated. Differentiation was achieved by resuspending THP-1 cells at 4 × 10^5 cells/mL in the cell culture medium with addition of PMA (phorbol-12-myristate-13-acetate; 20 ng/mL), and incubating them at 37 °C and 5% CO2 overnight. PMA was prepared as a stock solution (10 mg/mL) in ultrapure absolute ethanol. Stocks were kept at − 20 °C in the dark. Differentiated THP-1 cells were rinsed with PBS and detached by using Accutase® solution to harvest them.

On day 4, Macrophage-like cells and HMC-1 cells were added into the inserts (2.4 × 10^{5}cells/cm^2 and 1.2 × 10^5 cells/cm^2, respectively) with A549 and EA.hy926 cells to complete the tetra-culture system. The medium for the complete tetra-culture contained 1% FBS in order to avoid the extensive proliferation of HMC-1 cells. Once macrophage-like cells and HMC-1 cells were attached, the medium was removed from the apical compartment to allow cell model cultivation at the ALI for 24 h before exposure. The integrity and the quality of the cell layer on both side of the insert is checked for each insert before performing the exposure to be sure to have a uniform cell monolayer on both side of the insert. The presence of the surfactant in check on one insert randomly selected by using the Surfactant droplet test. The inserts can only be used when the previously mentioned parameters are validated. All model details and characterizations are described in the previous work by Klein et al. (2013).

2.5. Aerosol exposure and NP suspension preparation for the Vitrocell® cloud system

A Vitrocell® Cloud System (6-well model) was used to nebulize NP suspensions and expose our *in vitro* model. This system is designed for the dose-controlled and spatially uniform deposition of liquid aerosols, which maintains cells at 37 °C in an atmosphere at 100% humidity over 6 inserts. The exposures were carried out in two batches one after the other with the first batch composed of 6 inserts and the second batch composed of 3 inserts. This approach was performed for each biological replicates (N = 3). The exposure was performed by using groups of NP suspensions that were prepared in PBS 0.5X in order to obtain a deposition of 0.34 or 1.7 μg/cm^2. PBS 0.5X vehicle solution was used as Negative Control as demonstrated in previous studies using the same approach (Klein et al., 2017; Chary et al., 2019; Fizeșan et al., 2019). To allow the complete deposition of the liquid aerosols, exposure to the aerosol too place over a period of 15 min. During the exposure a custom-made ring was used to prevent any contamination of the basolateral side of the insert. Then, the tetra-culture was incubated for 24 h to compensate for any potential mediocre uptake of any of the cell lines or used nanoparticles. Therefore, all further analysis were done 24 h after the exposure. Each analysis was carried out on three different biological replicates obtained from three independent exposures.

2.6. Viability assay

Twenty-four hours after the exposure, the medium from the basolateral (BL) compartment was recovered and used for the LHD assay. A working solution of resazurin (400 μM) was prepared in CCM and added to both insert sides (apical and basolateral). The plates containing the inserts were incubated in a humidified atmosphere with 5% CO$_2$ at 37 °C for 2 h. Then, 200 μL of CCM with resazurin were transferred to a 96 well plate and the fluorescence was read by a Microplate reader (TECAN; Ex: 530 nm; Em:590 nm). Cell viability was calculated as a percentage compared to the Negative Control group using the formula: [(Sample Fluorescence Intensity – CCM Background) / (Negative Control Fluorescence Intensity– CCM Background) * 100]. The results show the average of three different biological replicates. This protocol had already been set up and applied to this coculture model in a previous work (Fizeșan et al., 2019).

2.7. Cytotoxicity assay

An aliquot of the BL medium that was recovered 24 h after exposure, was used to perform a cytotoxicity assay measuring Lactate Dehydrogenase's release (LDH) with the commercially available CytoTox-ONE™ (Promega) kit, following the manufacturer's instruction. 50 μL of the LDH-substrate mix were added to 50 μL of the BL medium and incubated for 10 min before adding 25 μL of the stop solution. For the positive control, cells were previously lysed using Triton X-100, and maximum LDH release was quantified in the same way. These measurements were only performed on the BL medium since no medium was present on the apical side as the system was at the ALI. The fluorescence was read by a Microplate reader (TECAN; Ex:530 nm, Em:590 nm). Cytotoxicity was calculated as a percentage compared to the negative control level of LDH release: [(Sample Fluorescence Intensity – CCM Background) / (Negative Control Fluorescence Intensity – CCM Background) * 100]. The results show the average of at least three different biological replicates. This protocol had already been set up and used for this coculture model in a previous work (Fizeșan et al., 2019).

2.8. AuNP uptake

Twenty-four hours after exposure, both insert sides were washed twice with PBS to remove non-internalized particles from the surface (Nahvi et al., 2022; Zhang et al., 2023). Cells were trypsinized, recovered with CCM, then cells were centrifuge 5 min at 300 g and supernatants were discarded to resuspended in PBS; 10 μL of the cell suspension was stained with Trypan Blue and counted with C-chip™ (NanoEntek) disposable haemocytometers. The cells were centrifuge again 5 min at 300 g, supernatants were discarded, and the cellular pellets were stored at − 20 °C until further steps could be carried out. To determine the total Au, samples were placed in tubes with 0.375 mL HCl (Optima, Fisher) and 0.125 mL HNO$_3$ (Optima, Fisher). The samples were digested in a heating block (Digiprep, SCP SCIENCE) for 120 min at 105 °C. Total concentrations were measured with a quadrupole ICP-MS (Nexion 300 s, PerkinElmer) equipped with a baffled cyclonic spray chamber and a conical nebulizer. The internal standards of the analytical masses were 197Au and 103Rh.

2.9. Transcriptomic analysis

Twenty-four hours after exposure, inserts were washed with PBS to remove non-internalized particles from the cell surface. Three biological replicates were performed for each treatment group. Using a lysis buffer (Buffer RLT, QIAGEN®) cells were disrupted and lysates were recovered to be frozen immediately in liquid Nitrogen and stored at − 80 °C until further processing. The total RNA was purified and stored at − 80 °C until the next step, following the manufacturer's protocol (QIAGEN® – RNA purification kit).

One μL of each single replicate was checked in terms of quantity and purity with the Nanodrop ND1000 spectrophotometer (Thermo Scientific, France) and another 1 μL of was used to verify the RNA integrity with the RNA Nano 6000 assay (Agilent Technologies, Belgium) using a 2100 Bioanalyzer (Agilent Technologies, Belgium). The RNA quality was considered acceptable, with RIN (RNA Integrity Number) values above 9 and a quantity higher than 100 ng.

cDNA libraries were constructed from 1 μg of RNA_{tot} extracted using the SMARTer® Stranded Total RNA Sample Prep Kit – HI Mammalian (TAKARA Bio, USA) following the manufacturer's instructions.

One μg of total RNA was depleted of rRNA using SPRI beads and the SMARTer® protocol. The total eluted RNA was used to synthesize the First-Strand cDNA using the SMARTer® Stranded oligonucleotides before being purified following the manufacturer's instructions. Indexing was performed using the Illumina Indexing Primer Set HT for Illumina. The enrichment step was carried out using 12 cycles of PCR. Subsequently, libraries were checked using a 2100 Bioanalyzer (DNA High sensitivity Kit) to evaluate the mean fragment size. The libraries were normalized according to the average size and qubit quantification, and pooled in equimolar concentration. The pooled library (4 nM) was sequenced using a paired end 2 × 75 cycle High Throughput kit on an Illumina NextSeq500 sequencer.

2.10. RNA Seq analysis

Raw sequences were deposited at the Sequence Read Archive (SRA) with the accession number GSE184990 (https://www.ncbi.nlm.nih.gov/geo/query/acc.cgi?acc=GSE184990). Raw data were processed using CLC Software (Genomics Workbench v. 9.0.1). Sequences were filtered as follows: for sequences > 75 bps, the sequence quality score was left as the default value (0.05) and the maximum number of ambiguities was set to 0. Then, a hard trim of 10 bps at the 5′ end and 0 bps at the 3′ end was carried out, resulting in a final sequence average length of 65 bps. The parameters used for the mapping of the reads toward the human genome reference (GRCh38.p13) were: wording size 20, bubble size 50 and minimum counting length 300.

The data analysis software R was run on the counting table mostly following the EdgeR pipeline (Chen et al., 2016).

The results were then filtered and normalized, and the new library was considered for all further analysis. The normalization of the results was performed using the calcNormFactors function (EdgeR). A set of normalization factors was calculated, one per sample, in order to eliminate the composition biases between different libraries. The normalization was carried out based on RPKM values. Once the effective library size was obtained, the analyses were conducted in this library size replacing the original one. The results were normalized based on the CPM and no significant differences were founded before and after the normalization.

We performed the glmQLFTest progressively, allowing us to identify differential expression based on statistical significance. After obtaining the Differentially Expressed Genes (DEG) from each contrast of interest, the results were screened again. We kept only DEG with a P-value < 0.01 and $-1 > Log_2FC > 1$ in order to be stringent and to consider strongly DEG compared to the control groups (Ctrl_AP and Ctrl_BL). The two thresholds were chosen to consider the complexity of the tetra-culture system. Indeed, the system contains different cell types at different densities with a response that may vary greatly for each cell type and the possibility of diluting the response of the less present cell type of the system. Therefore, measuring and reporting these changes could provide information of great importance (St. Laurent et al., 2013).

Due to the use of stringent cut-off parameters to filter out the DEG no further adjusting methods were used (Vidgen and Yasseri, 2016).

In total, 13 contrasts were made (Table 2); first, Ctrl_AP and Ctrl_BL were compared, each treatment was compared to the related control.

Table 1

Summary of the number of reads before ('raw reads') and after filtering out low-quality reads ('clean reads'), as well as the number of trimmed reads mapped on the human reference genome (HG19) (mean ± SE, N = 3). [a]

	Ctrl	Spheres 0.34 μg/cm²	Spheres 1.7 μg/cm²	Rods 0.34 μg/cm²	Rods 1.7 μg/cm²	Stars 0.34 μg/cm²	Stars 1.7 μg/cm²
Apical Side							
Number of raw reads	13.50 ± 2.17	14.05 ± 0.30	13.19 ± 1.38	14.20 ± 0.98	15.50 ± 3.26	11.46 ± 3.00	14.38 ± 2.16
Number of reads clean reads	13.49 ± 2.16	14.04 ± 0.30	13.18 ± 1.37	14.20 ± 0.98	15.50 ± 3.26	11.45 ± 3.00	14.37 ± 2.16
Number of mapped reads	10.55 ± 2.68	10.61 ± 1.81	11.04 ± 0.81	12.51 ± 1.44	12.10 ± 1.86	10.03 ± 2.23	11.74 ± 3.26
Basolateral Side							
Number of raw reads	13.50 ± 0.59	11.03 ± 4.90	13.51 ± 2.68	14.58 ± 3.87	15.28 ± 1.83	14.24 ± 2.21	13.99 ± 0.32
Number of reads clean reads	13.49 ± 0.59	11.03 ± 4.90	13.50 ± 2.68	14.58 ± 3.87	15.27 ± 1.83	14.23 ± 2.21	13.98 ± 0.32
Number of mapped reads	10.55 ± 0.64	9.31 ± 4.74	12.10 ± 2.63	11.79 ± 3.26	13.90 ± 1.86	11.00 ± 3.83	11.13 ± 0.55

[a] The number of reads are indicated as 10^6 values.

Table 2
Number of differentially expressed genes (DEG) by contrasts.

Contrast	Number of DEG	Down regulated	Up regulated
1.Ctrl_AP vs Ctrl_BL	4324	2519	1805
2.Ctrl_AP vs Rods_AP_0.34 µg/cm^2	48	14	34
3.Ctrl_AP vs Rods_AP_1.7 µg/cm^2	46	12	35
4.Ctrl_AP vs Spheres_AP_0.34 µg/cm^2	31	20	11
5.Ctrl_AP vs Spheres_AP_1.7 µg/cm^2	26	9	17
6.Ctrl_AP vs Stars_AP_0.34 µg/cm^2	36	24	12
7.Ctrl_AP vs Stars_AP_1.7 µg/cm^2	38	24	14
8.Ctrl_BL vs Rods_BL_0.34 µg/cm^2	37	20	17
9.Ctrl_BL vs Rods_BL_1.7 µg/cm^2	24	9	15
10.Ctrl_BL vs Spheres_BL_0.34 µg/cm^2	33	19	14
11.Ctrl_BL vs Spheres_BL_1.7 µg/cm^2	63	49	14
12.Ctrl_BL vs Stars_BL_0.34 µg/cm^2	35	19	16
13.Ctrl_BL vs Stars_BL_1.7 µg/cm^2	31	22	9

[a]Down-regulated and up-regulated DEG regarding their respective controls with Log$_2$FC > 1 or < −1 with *P*-value < 0.01. For the comparison of the two compartments, the selected reference condition was the apical compartment.

2.11. Statistical analysis

Each experimental condition was defined by mean ± SE (biological replicates: N = 3). Data on tetra-culture viability and cytotoxicity are reported as average percentages compared to the control group plus SE; statistical analyses were performed by One Way ANOVA followed by the paired t-test. Uptake data are reported as mean values ± SE and the statistical analyses were performed by non-parametric Kruskal-Wallis test followed by an unpaired Dunn's test. The analyses were performed using Microsoft Office Excel 2010 and R Studio Software (RStudio Team (2020). RStudio: Integrated Development for R. RStudio, PBC, Boston, MA URL http://www.rstudio.com/).

3. Results

3.1. AuNP characterization

Fresh suspensions were characterized by UV–vis absorption spectroscopy, Transmission Electron Microscopy (TEM), Dynamic Light Scattering (DLS) and Enhanced Dark Field Microscope (EDFM, Cyto-Viva®) (Additional file 1). The following dimensions were obtained by TEM: 61.33 ± 0.34 nm for GNPs, 18.44 ± 6.4 nm (width) and 68.3 ± 10.3 nm (length) for GNRs and 63.43 ± 2.35 nm for GNSs. These values correspond to the dimensions of the gold cores, not taking into account the organic ligand shell around the NPs. In the previous work using the same batch of AuNPs, their zeta-potential were measured: GNPs − 33.2 ± 0.6 mV, GNRs − 22.9 ± 0.6 mV, GNSs − 26.4 ± 0.2 mV (Supplementary material Talamini et al., 2017). The HIM analysis confirmed the different shapes of the AuNPs (Fig. 1a-c). The NP suspensions were also prepared in a surfactant (poractant alfa), in order to evaluate the effect of the surfactant on size distribution since the alveolar type-II cells (A549) were able to produce it when left at the ALI.
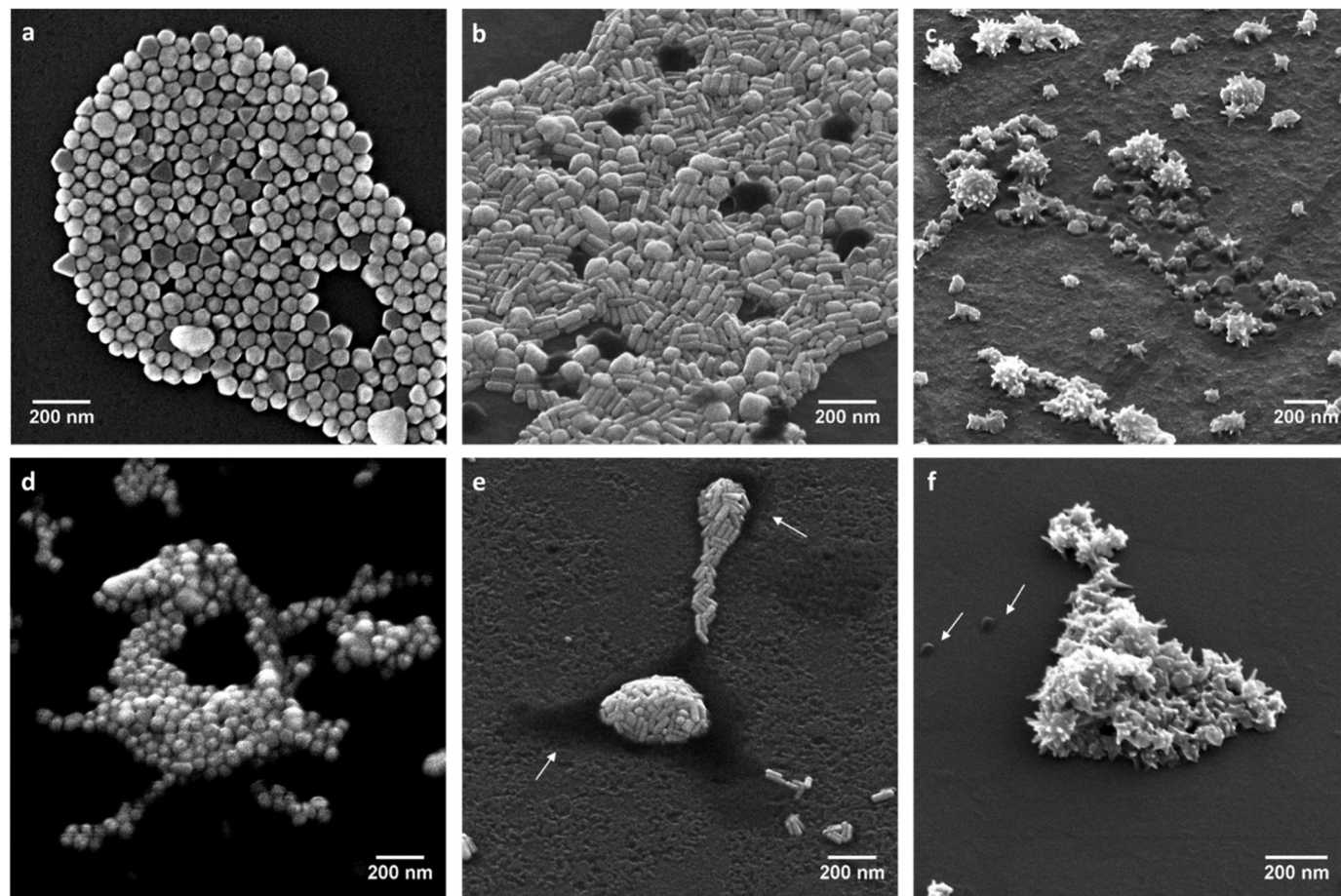

Fig. 1. AuNPs suspensions observed with HIM microscope. Images of suspensions prepared in MilliQ water (0.5 mg/mL, a: GNPs, b: GNRs and c: GNSs) and the same suspensions incubated for 1 h in poractant alfa diluted with PBS 0.5X (concentration corresponding to 0.34 µg/cm^2 for, d: GNPs, and 1.7 µg/cm^2 for e: GNRs and f: GNSs) by HIM (scale bar: 200 nm). White arrows may indicate the presence of surfactant (e and f).

When suspended in the lung surfactant, the AuNPs agglomerated and it was possible observe a halo on the stub surface (white arrows, Fig. 1e-f) which most probably correspond to phospholipids, the major component of the surfactant.

3.2. Tetra-culture alveolar model viability

The tetra-culture alveolar model was exposed to nebulized AuNPs in a Vitrocell® Cloud system. The cells on the AP side were maintained at the ALI for 24 h before the exposure. The NP suspensions were prepared in order to obtain theoretical concentrations of 0.34 or 1.7 µg/cm^2, considering the entire amount of nebulized AuNPs deposited. As the

negative control, a solution of diluted (0.5X) PBS was nebulized. The viability of the tetra-culture was evaluated 24 h after exposure to the incubating cells (both sides) using a solution of resazurin in CCM and measuring the fluorescence of the metabolized compound.

After 24 h, the AP cell viability did not show any statistically significant difference after any of the exposures compared to the negative control and among treatments (Fig. 2a).

Treatment with AuNPs (all shapes and concentrations) did not have any statistically significant effect on the cell viability of the endothelial cells as compared to the negative control (Fig. 2b).

In order to evaluate the cytotoxicity of the AuNPs, Lactate Dehydrogenase (LDH) release was analysed in the BL medium recovered 24 h
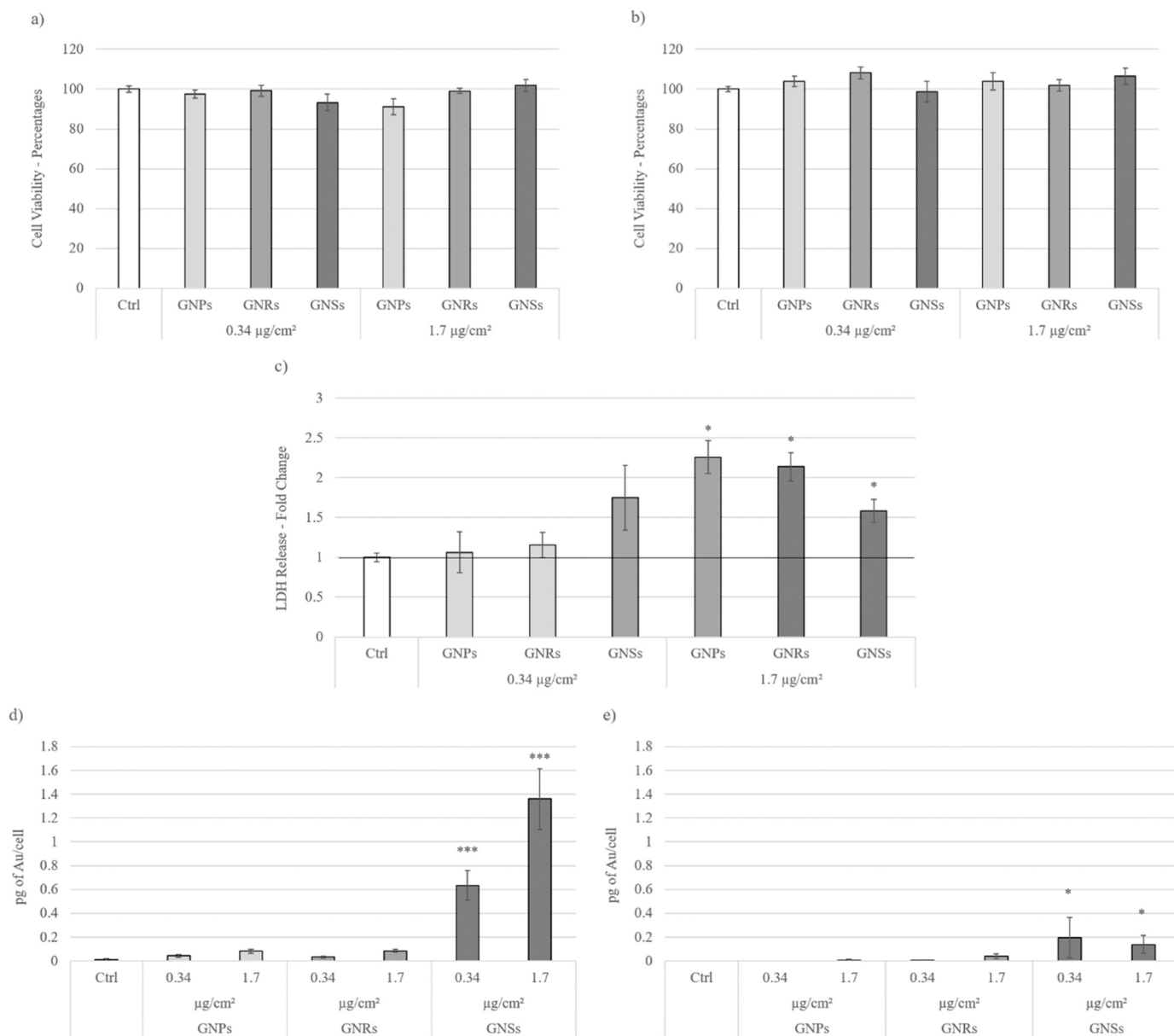

Fig. 2. Tetra-culture viability assay, evaluation of cytotoxicity, AuNP uptake. Cell viability was evaluated by measuring the fluorescent signal of the metabolized resazurin after 24 h of exposure to PBS (Ctrl) and AuNPs (0.34 – 1.7 µg/cm^2) in the Apical (a) and Basolateral (b) side of the model. Data is expressed as mean ± SE (N = 3); no significant differences were observed (p < 0.05, One Way ANOVA + paired t-test). Histograms (c) show the levels of LDH (Lactate Dehydrogenase) in the basolateral compartment after 24 h of exposure to PBS (Ctrl) and AuNPs (0.34 – 1.7 µg/cm^2) in order to evaluate the cytotoxicity of the treatments. Data is expressed as mean ± SE (N = 3); *statistically significant increase versus negative control (P < 0.05, One Way ANOVA + paired t-test). Quantification of the amount of gold in the apical cells (d), and in the cells of the basolateral (e) side of the tetra-culture model. Data is expressed in picograms of gold per cell (pg/cell); the pg of gold were normalized based on the cell number recovered in each insert compartment. Values under the lower instrument limit of detection were considered as null values. Statistical analysis was performed using the Kruskal-Wallis test followed by Dunn's test versus the control (* P-value < 0.01; ** P-value < 0.001; *** P-value < 0.0001). Results are expressed as mean ± SE; N = 3.

after treatment (Fig. 2c) and a statistically significant increase (*P*-value < 0.05) in the levels of LDH was observed after exposure to the highest dose (1.7 µg/cm^2) of all AuNPs.

3.3. AuNP uptake by co-culture (A549, macrophage-like cells and HMC-1) on the apical side and transport through the model to the endothelial cells on the basolateral side

Au NP uptake was evaluated measuring the amount of Au in the compartment cells by ICP-MS from the apical and basolateral side separately. To avoid false positive results due to the possible presence of NPs on the cell surface the co-coculture was washed several times with PBS before collecting the cells. However, it is important to mention that strongly attached AuNP may still be present after washing the apical part. The AP and BL compartments were analysed separately in order to evaluate not only the uptake by the entire tetra-culture (sum of Au on the AP side + BL side, data not shown), but also the possible transport of NPs in the BL compartment, which had never before been directly exposed (endothelial cells, Fig. 2e).

We observed the uptake of NPs on the AP side 24 h after exposure (Fig. 2d). However, a clear dose-dependent statistically significant (*P*-value < 0.0001) uptake was only observed in cells exposed to GNSs. Au was also detected in the BL compartment (Fig. 2e), confirming that there was a measurable passage of GNSs and GNRs through the insert membrane from the different apical cell lines. Interestingly this passage was higher for the GNSs. The localization of those translocated AuNPs in the BL compartment was investigated by HIM, but NPs were not detected (data not shown).

3.4. Transcriptomic analysis

In order to obtain a global vision of gene expression in the two parts of the in vitro system exposed to the different AuNPs, we performed a large-scale transcriptomic analysis of the AP and BL sides 24 h after exposure (0.34 and 1.7 µg/cm^2). A total of 288,823,954 and 283,365,614 reads were obtained from the sequencing of the 21 cDNA libraries of the AP and BL side, respectively (Table 1). From these 572,189,568 reads 571,997,780 reads were kept after filtering out the low-quality reads corresponding to 99.97% of the raw reads for all libraries. Those filtered reads were then mapped against the human reference genome HG19 resulting in the mapping 81.8% of the AP reads and 84.3% of the BL reads.

Then, the poorly covered genes were filtered with Count Per Million (CPM) > 0.9 in each library and a sum of CPM > 3, and for all three biological replicates a total number of 19,702 genes went through the two filtering steps.

To reduce any redundant information, we performed Principal Component Analysis (PCA) (Fig. 3). All treatments related to the AP side were arranged on the left side of the plot, whereas the dots referring to the BL side are on the right side. This PCA analysis reveals that the different treatments cluster in two different groups. These two groups are related to either the AP cells or the BL. Furthermore, in the clusters, the exposed cells group together with the control condition, showing a similar gene expression profile with regard to their respective negative control.

The next step consisted of determining the DEG between the experimental treatments and their respective controls (Table 2; Additional file 2). In general, the different comparisons identified a total number of about 100 impacted genes with the exception of four comparisons, which only identified about 60 DEG (Ctrl_AP vs Spheres_AP_1.7 µg/cm^2; Ctrl_BL vs Rods_BL_1.7 µg/cm^2; Ctrl_BL vs both Stars_BL_0.34 µg/cm^2 and Stars_BL_1.7 µg/cm^2). An additional comparison was performed between the two control conditions (AP and BL side) identifying more than 4300 DEG, which is coherent with the fact that in this case, the comparison was performed on two different cell assemblies corresponding to the alveolar epithelium (AP side) and the capillary endothelium (BL side).

For more detail on DEG, please refer to Additional file 3 from which the first 15 DEG with the highest FC for each contrast were extracted (Table 3). Looking at the list of the top 15 DEG some common features
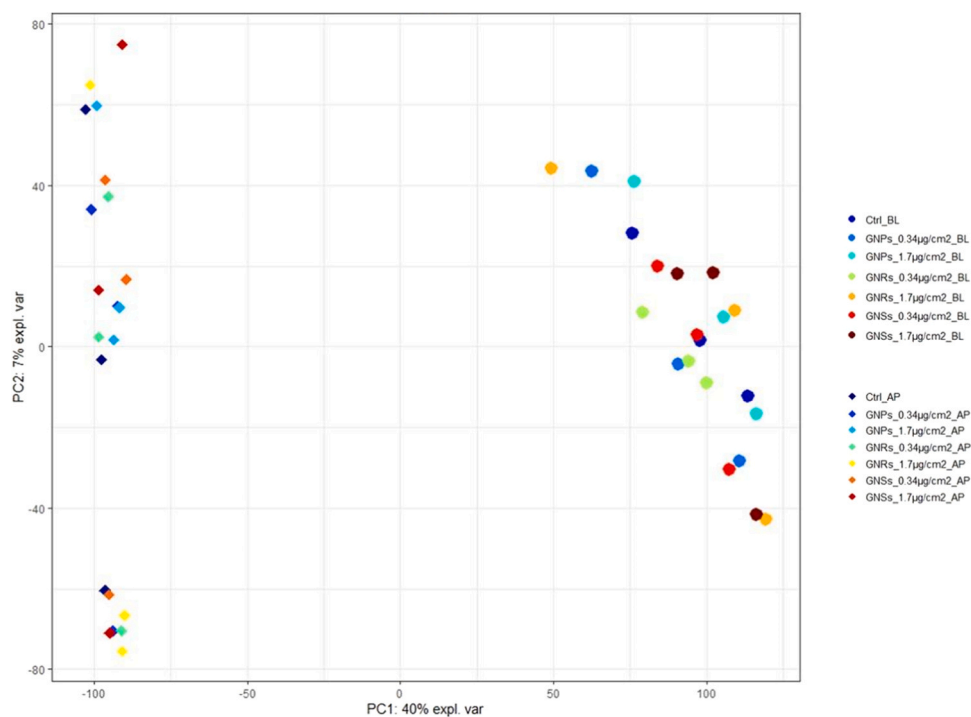

Fig. 3. Principal component analysis (PCA). Each color represents a single treatment for each biological replicate (N = 3). On the left all the treatments referring to the apical side are clustered, and on the right all treatment referring to the basolateral side. The samples are clustered according to the value distribution of component 1 and component 2.

Table 3

Summary of the top 15 DEG for each comparison.

Ctrl AP vs Rods AP 0.34 μg/cm²		Ctrl AP vs Rods AP 1.7 μg/cm²		Ctrl AP vs Spheres AP 0.34 μg/cm²		Ctrl AP vs Spheres AP 1.7 μg/cm²		Ctrl AP vs Stars AP 0.34 μg/cm²		Ctrl AP vs Stars AP 1.7 μg/cm²	
TBC1D3H	7.73	TBC1D3H	7.69	TBC1D3H	7.93	PLGLB2	6.92	PCDHA1	6.40	PCDHA1	6.11
PCDHA1	5.90	OTOGL	5.46	GOLGA8N	5.72	GOLGA8N	5.08	SPATA3-AS1	5.73	PLGLB2	5.73
PCDHGC3	5.02	GPR146	5.21	GPR146	4.73	HTN3	4.38	PCDHGC3	4.91	OTOGL	5.66
SPATA3-AS1	5.02	GOLGA8N	4.87	RGPD1	4.68	GPR146	4.18	CCNYL2	4.74	SPATA3-AS1	5.52
FOXC2	4.98	PCDHGC3	4.65	RNVU1-14	3.60	PLA1A	2.69	GPR146	4.32	RGPD1	4.41
GPR146	4.72	MEI4	3.09	LRRC71	3.25	NPIPB11	2.53	SLC23A3	-2.67	TMEM204	4.19
RGPD1	4.64	SLITRK1	3.07	PLA1A	3.24	GBX2	2.50	SH2D4B	-2.91	PCDHB12	3.43
OTOGL	4.41	RNVU1-14	2.89	LIPM	-3.90	SCARF2	-2.46	PCDHB14	-3.01	TMEM145	-2.67
RASAL2-AS1	-4.33	PRRX1	2.80	CLEC12B	-4.46	ARAP1-AS2	-3.14	PDC	-3.47	C1QTNF8	-2.70
CLEC12B	-4.46	IL12A	-2.86	RIMBP3C	-4.52	SCHIP1	-3.93	GLYATL2	-3.81	GPT	-2.99
USP32P2	-5.00	C15orf62	-3.77	SLC5A4	-5.26	LINC01013	-4.73	CLEC12B	-4.46	SLC23A3	-3.00
PTGIS	-5.13	MAMDC2	-4.10	ACP5	-5.31	MYBPH	-5.18	PLA2G4B	-6.04	MEIG1	-3.63
PPP1R36	-5.24	CLEC12B	-4.46	PITRM1-AS1	-5.97	PRR5-ARHGAP8	-6.24	NUTM2G	-6.31	SLC5A4	-5.26
NSG1	-5.72	LINC00475	-4.98	RBFADN	-7.09	SENP3-EIF4A1	-7.03	MSH5-SAPCD1	-6.74	LRRD1	-5.88
ASB3	-8.03	KCNJ13	-5.72	ASB3	-8.03	ASB3	-8.03	SERF1A	-8.36	SENP3-EIF4A1	-7.03
Ctrl BL vs Rods BL 0.34 μg/cm²		**Ctrl BL vs Rods BL 1.7 μg/cm²**		**Ctrl BL vs Spheres BL 0.34 μg/cm²**		**Ctrl BL vs Spheres BL 1.7 μg/cm²**		**Ctrl BL vs Stars BL 0.34 μg/cm²**		**Ctrl BL vs Stars BL 1.7 μg/cm²**	
SAA1	5.73	TNFRSF6B	6.15	SNAP91	7.86	TNFRSF6B	6.23	SNAP91	7.93	AMIGO1	5.19
CRB3	4.91	CPN1	5.72	ARL14	5.42	FBLN7	5.56	PGA3	5.36	CX3CR1	4.63
AP3B2	4.68	SPDYE2B	5.24	LAD1	5.30	RNASE6	5.20	AMIGO1	4.92	MUC6	4.35
TMEM151A	4.57	CRB3	4.88	HSPA6	4.21	NPHS1	-5.23	GABRG2	4.78	GLTPD2	-2.50
CX3CR1	4.55	CX3CR1	4.55	VWDE	3.57	MYLK-AS2	-5.26	FBLN7	4.74	AMDHD1	-2.88
CRLF2	3.99	EFNB3	4.53	PLEKHB1	3.04	MARVELD3	-5.45	SCG3	4.74	ZNF497	-2.95
SYNDIG1	-3.52	FBLN7	4.13	FAM71E1	2.71	MNX1-AS1	-5.52	SPTSSB	-4.84	HCG27	-3.39
ADRA2C	-4.77	SEPT7P9	3.05	LYNX1	-2.51	GAPDHS	-5.63	AIFM3	-5.20	CHDH	-3.95
SPTSSB	-4.84	VWDE	2.97	CCDC78	-2.71	SYCP3	-5.72	ACVR1C	-5.37	LINC00887	-4.91
ESRG	-4.97	SYNDIG1	-2.91	PRR15L	-3.38	SLC25A41	-5.78	ALOX12P2	-5.42	TP73	-5.08
TSPAN2	-5.06	ZKSCAN7	-3.90	GRM1	-3.63	GRB7	-5.85	HEXA-AS1	-5.43	MNX1-AS1	-5.52
ZNF93	-5.18	SYCP3	-3.93	CDH7	-4.26	CKLF-CMTM1	-6.10	GOLGA2P5	-5.46	SLC17A9	-5.55
HEXA-AS1	-5.43	COL1A1	-4.31	CPLX1	-5.41	GP6	-6.26	ADAMTS15	-5.66	ZNF239	-5.58
GJA9	-5.95	ANXA8	-5.00	KCNMB2	-5.50	FSBP	-7.28	JMJD7-PLA2G4B	-6.04	NRL	-5.68
PRR15L	-6.65	FAM66E	-6.93	ASH1L-AS1	-6.04	HOXB-AS3	-8.20	ZNF671	-6.13	PRR15L	-6.65

[a]The reported genes have the highest |log$_2$FC=(reported in the table) and *P*-value < 0.01. The red genes are induced genes, whereas the blue ones are repressed genes.

are observable among the treatments.

On the AP side, we mainly observed an alteration in the expression of genes involved in processes related to the immune cells (*CLEC12B, GPR146, PCDHGC3* for GNRs; *GPR146* and *PLAIA1* for GNPs; *PCDH12/14* for GNSs). In addition, most DEG contain genes related to the plasma membrane (*PCDHGC3* and *TBC1D3H* for GNRs; *PCDHA1* and *PCDH12/14* for GNSs) or the vesicles pathways (*TBC1D3H* for GNRs). After treatment with GNSs, a different expression of *SLC23A3* was observed.

Most DEG on the BL side were also genes related to the enhancement of immune cells (*CRB3* and *CX3CR1* for GNRs) or genes related to vascular development, angiogenesis and/or vascular remodeling (*AMIGO* family for GNSs).

The DEG were compared between the contrasts and a few common genes were obtained for the two exposure concentrations and the different shapes. In addition, very few common impacted genes were found between the different treatments that did not allow the identification of a common pattern linked to the AuNPs exposure.

As a next step, Gene Ontology (GO) assignments were used to classify the functions of the differentially expressed cell transcripts into biological processes, molecular functions and cellular components for both the AP and BL compartments for each exposure condition (Additional file 4). Globally, the different exposure conditions showed a similar profile of GO annotation within the same compartment. In the AP and BL compartment, the number of genes at level 3 of GO terms in the biological process reveal that the genes were mainly involved in the regulation of the cellular process, organic substance metabolic process,

primary metabolic process, cellular metabolic process and nitrogen compound metabolic process, with anatomical structure development only present in the AP compartment. Concerning the molecular function, the genes were mainly involved in protein and ion binding without any differences between the two compartments.

4. Discussion

Our study describes the effects of physicochemical properties of three different types of AuNPs on a complex in vitro human alveolar model. The complexity of our model represents a good compromise for predicting the effects of NPs upon inhalation. AuNPs were nebulized using the VitroCell® Cloud System at the ALI.

The effects of our AuNPs (GNPs, GNRs and GNSs) were evaluated 24 h after exposure to two different doses (0.34 and 1.7 μg/cm²) in terms of viability, cytotoxicity, uptake, exchange between compartment and global gene expression. A previous study performed on AgNPs revealed a deposition efficiency of 65% while using a Vitrocell™ Cloud system (Fizeşan et al., 2019). The deposition efficiency corresponds with the measurement of 68% deposition efficiency of a nebulized fluorescein-spiked saline solution (Ding et al., 2020). Taking into consideration these deposition efficiencies, the estimated exposures in the present study are 0.2 and 1.1 μg/cm². Given the high intake of air (> 20 m³/day) and the large surface area (75–150 m²) of the respiratory tract, the inhaled ENMs are deposited efficiently in the alveoli. Indeed, the integrity of the alveolar barrier is the main concern due to the

deposition of small particles. A dose of 0.05 μg/cm^2 already represents an acute exposure dose in a high-exposure occupational scenario (Fizeşan et al., 2019). This observation brings us to the conclusion that any effect observed in the present study is biologically relevant and could be related to the biological effect of different inert ENM shapes. Under such exposure conditions, our study revealed that neither compartment (AP and BL) was affected in terms of cell metabolic activity as no significant differences could be observed 24 h post-treatment (Fig. 2). However, it was evident that AuNPs had an effect on cell membrane integrity as LDH leakage occurred (Fig. 3). LDH is an oxidoreductase enzyme involved in cellular respiration, and catalyzes the transformation of pyruvate into L-Lactate, involving the reduction of NADH to NAD$^+$. This enzyme is ubiquitous and quite stable. It is often used as a marker of cytotoxicity because its release provides an index of compromised cell membrane and, consequently, cell death (Riss et al., 2004).

A significant increase in the LDH level was observed after exposure to the highest dose (1.7 μg/cm^2) of all AuNPs. A similar observation was observed on the same *in vitro* system 24 h after exposure to different AgNPs (5 μg/cm^2) (Fizeşan et al., 2019).

AP and BL insert sides were considered separately for the uptake (Fig. 2d, e). Our results demonstrate that all AuNPs were taken up or strongly attached in a dose-dependent manner by the cells present on the AP side (A549, HMC-1 and Macrophage-like cells). Significant amounts of gold were found 24 h after exposure to GNSs, considering both doses tested. The uptake was dose-dependent, especially for GNSs, for which the trend is clearer and stronger. GNPs and GNRs are taken-up at a much lower rate (at least 15 times less) than GNSs. This shows the importance of the NP shapes regarding their interaction with the cells (adhesion and/or endocytosis). And those observations are aligned with previous studies showing that among the different NPs parameter the size and shapes are extremely important. In the present case, the difference between the Au NPs is the shape as their sizes are in the same range. But the shape itself is known to influence the NPs corona and potentially their aggregation degree that are two key parameters impacting their cellular uptake rate and internalization behavior. In addition to this parameter, the various shapes have been demonstrated as a key parameter for penetration capability with efficacy penetration of NPs across the cellular multicomponent lipid layer higher for rod than sphere (Gupta et al., 2020). It is also worth mentioning that the internalization process is divided into three steps: ligand–receptor binding, invagination and wrapping stages. And the stronger the ligand-receptor binding energy is, the higher the chance of initiating the endocytosis will be as the NPs maximize their contact area with the membrane. This confirms that there is a different ability of the NPs to enter cells in the AP side based on their physicochemical properties. In addition, in the BL side a statistically significant amount of gold per cell was only observed after exposure to GNSs. This presence of GNS in the basolateral part can be link to a passive diffusion from the apical part to the basolateral part as the GNS may pass between the cells as the A549 are unable to form tight junction. However, this possibility, is highly unlikely to be the case as no GNPs and GNRs are detected in the basolateral compartment. The second possibility is a vesicle-mediated uptake, transport and release at the basolateral side bring GNSs in contact with the endothelial cells on the basolateral side. This transport is much more important for GNSs than GNPs and GNRs, which is probably directly related to the higher uptake of GNSs by the cells in the AP side. There was some indication that AuNP transport was shape- and dose-dependent although the low amounts detected in the BL compartment, as well as the high standard deviation do not allow us to reach a final conclusion.

These results are very interesting because they clarify that there is a distinct translocation of particles through the cells and the insert membrane. This gives further confirmation of the presence of intercellular exchange and communication among the different cell lines. This report shows that our *in vitro* tetra-culture model is suitable for uptake and translocation studies of inhalable NPs.

The Gene Ontology (GO) analysis of the AP compartment's DEG revealed a different pattern with GNRs and GNSs impacting a larger number of genes related to the cell membrane than to GNPs. We can speculate that GNSs and GNRs could have physically altered the cell membrane integrity, whereas the GNPs, with their smooth edges, do not induce such effects. Holes or breaches in the membrane facilitated a major leakage of the cell content, LDH included. A similar correlation between LDH release and NP physical properties has previously been claimed (Forest et al., 2017). Comparing differently shaped CeO$_2$NPs, the authors found statistically significant different LDH levels: sharpened NPs caused a higher release than octagonal ones. However, it is extremely difficult to relate effects to shape, as a change in shape also generally causes other physicochemical properties, such as NP volume, NP surface, and NP surface chemistry, to change (Xu et al., 2018).

After exposure to GNPs, GNRs and GNSs, the presence of DEG was observed, related to the enhancement of immune cells. These genes (*CLEC12B*, *GPR146*, *PCDHGC3* for GNRs; *GPR146* and *PLAIA1* for GNPs; *PCDH12/14* for GNSs) were expressed differentially after any treatment on the AP side. It is known that NPs can modulate the immune system, and for this reason, they are used in immunotherapy as a form of drug delivery (Fan et al., 2023).

The AuNP uptake was evaluated using the ICP-MS technique (Fig. 2d, e). Several authors assessed the influence of the physicochemical properties of NPs on their uptake (Murugan et al., 2015; Xu et al., 2018). The level of cellular uptake does not simply depend on dimension, surface area or charge, but also on shape (Niikura et al., 2013; Talamini et al., 2017).

It has been claimed that, because of their sharp surface structures, gold nano-stars could easily disrupt the endosomal membranes of human liver carcinoma cells and accumulate in the cytoplasm for long periods, regardless of their surface composition, charge, material or size (Chu et al., 2014). Alternatively, nano-spheres could enter cells via endocytosis and reside in the endosomes, where they would adapt to the organelle maturation or be excreted by exocytosis. Other researchers (Favi et al., 2015) hypothesized that the potential mechanism of cell death caused by nano-stars is that NPs enter the cells via endocytosis (Chu et al., 2014), concentrate in the nuclei (Romero et al., 2014) and cytoplasm (Dam et al., 2012; Chen et al., 2013), and induce a dose-dependent cell death via mechanical damage (Kodiha et al., 2015). A physicochemical and time-dependent cellular uptake was observed; the cellular uptake of PEGylated-Gold nano-triangles was the highest, followed by PEGylated-Gold nano-rods and PEGylated-Gold nano-stars (Xie et al., 2017). These results suggest that NP properties play a key role in cellular uptake, even if these observations are different from ours. The difference with our results might be due to the biological model: in Talamini et al. (2017), *in vivo* exposure was done intravenously whereas in the present work, the exposure was performed on an *in vitro* model at the ALI.

There are reports that show that the effects were not related directly to the shape of AuNPs, but rather to the different surface treatments, which had to be used to obtain the different NP shapes (Chakraborty et al., 2018; Gharib et al., 2019). For instance, to synthetize AuNPs of different shape, toxic surfactants often need to be used, such as cetyltrimethylammonium bromide (CTAB) for the synthesis of gold nano-rods, and thus toxic effects may be related to this particular surface coating rather than due to the shape (Soliman et al., 2015).

While shape clearly influences the NP-cell interaction, it is hard to unequivocally relate this parameter to the biological effects. This is due to the entanglement of different physicochemical parameters (Xu et al., 2018). Although in the present study GNPs, GNRs, and GNSs had a similar size in one dimension, and had different shapes, other physicochemical parameters were affected. For example, the three different AuNPs do not possess the same volume per NP, i.e. they comprise different amounts of Au atoms and do not have the same surface area per NP, e.g. the GNSs have a larger surface than the GNPs, which may play a role in photocatalytic properties. The results shown here thus

demonstrate clearly that the three NPs with different physicochemical properties have a different impact on our tetra-culture alveolar model. However, this impact cannot be related only to shape, since different shapes bring about changes in the physicochemical properties.

As expected, the AuNPs exposure did not induce severe lethal adverse effects, however, the parameters evaluated (viability, cytotoxicity, gene expression) revealed some biological effects. The effects are different for the three different types of AuNPs and show that outcomes depended on their physicochemical parameters. GNPs caused cytotoxicity at the highest dose, and different gene expression levels suggest that mainly the immune cell were impacted. They did not cause any specific or severe damage to the cells. GNRs led to an increase in cytotoxicity (highest dose). In addition, they caused changes in the expression levels of genes related to immune cells; we also observed DEG related to the membrane and vesicles. GNSs increased the level of LDH (both doses). Moreover, changes in the level of expression of genes involved in immune cell enhancement and cell membrane were observed.

The effects induced by different particles on the BL side appear similar, although the GNPs impacted a larger number of genes. The gene expression profile seems to emphasize stronger biological impacts on the AP side, with a higher number of impacted genes for the GNRs and GNSs than for GNPs.

5. Conclusion

In our study, the complex *in vitro* tetra-culture model, previously developed in our lab, was used to study the adverse effects of three different types of AuNPs (GNPs, GNRs and GNSs).

Although the different AuNPs did not have a significant effect on the co-culture, the biological response of such a complex *in vitro* system was efficiently modulated by the different NPs, likely as a consequence of a complex cellular interplay and NP translocation through the epithelial and endothelial layers of the lung alveolar model. Moreover, the transcriptomic analyses suggest that cellular dysfunctions related to the regulation of the cellular process and cellular ultrastructure may play a role in sub-acute or chronic exposure to AuNPs, raising concerns about their safe use over prolonged periods. The induction of slightly different effects confirms the importance of the physicochemical properties in driving NP-cell interactions and the suitability of the co-culture system to address biological effects of chemical able to reach alveoli. However, the system as clear limitation in term of investigating transport across the alveoli septum as the present model doesn't have a tight epithelium due to used cell lines.

Author contributions

MS planned and performed the experiments, performed the data evaluation and produced figures and tables. TS performed the EDFM analysis, planned and supervised the experiments at the ALI and the reporting of results. PB supervised the general experimental planning. AC supervised the general experimental planning. IN performed the ICP-MS analysis. RH performed the sequencing analyses. JNA performed the HIM analyses. BP produced and characterized the nanoparticles. MGS produced and characterized the nanoparticles. WJP produced and characterized the nanoparticles. PM supervised the general experimental planning. ACG supervised the daily work, the general experimental planning and the reporting of results. SC planned and supervised the molecular biological experiments and the related bioinformatics approaches.

All authors commented critically on earlier drafts of the manuscript. All authors read and approved the final manuscript.

Declaration of Competing Interest

The authors declare that they have no known competing financial interests or personal relationships that could have appeared to influence the work reported in this paper.

Data availability

The link to the transcriptomic data used in this article is mentioned in the Material and methods section.

Appendix A. Supporting information

Supplementary data associated with this article can be found in the online version at doi:10.1016/j.etap.2023.104353.

References

Blank, F., Rothen-Rutishauser, B.M., Schurch, S., Gehr, P., 2006. An optimized in vitro model of the respiratory tract wall to study particle cell interactions. J. Aerosol Med. 19, 392–405.

Bodelón, G., Costas, C., Pérez-Juste, J., Pastoriza-Santos, I., Liz-Marzán, L.M., 2017. Gold nanoparticles for regulation of cell function and behavior. Nano Today 13, 40–60.

Braakhuis, H.M., Kloet, S.K., Kezic, S., Kuper, F., Park, M.V.D.Z., Bellmann, S., van der Zande, M., Le Gac, S., Krystek, P., Peters, R.J.B., Rietjens, I.M.C.M., Bouwmeester, H., 2015. Progress and future of in vitro models to study translocation of nanoparticles. Arch. Toxicol. 89, 1469–1495.

Braakhuis, H.M., Giannakou, C., Peijnenburg, W.J., Vermeulen, J., van Loveren, H., Park, M.V., 2016. Simple in vitro models can predict pulmonary toxicity of silver nanoparticles. Nanotoxicology 10, 770–779.

Butterfield, J.H., Weiler, D., Dewald, G., Gleich, G.J., 1988. Establishment of an immature mast cell line from a patient with mast cell leukemia. Leuk. Res. 12, 345–355.

Chakraborty, I., Feliu, N., Roy, S., Dawson, K., Parak, W.J., 2018. Protein-mediated shape control of silver nanoparticles. Bioconjug. Chem. 29, 1261–1265.

Chary, A., Serchi, T., Moschini, E., Hennen, J., Cambier, S., Ezendam, J., Blömeke, B., Gutleb, A.C., 2019. An in vitro coculture system for the detection of sensitization following aerosol exposure. Altex 36, 403–418.

Chen, H., Zhang, X., Dai, S., Ma, Y., Cui, S., Achilefu, S., Gu, Y., 2013. Multifunctional gold nanostar conjugates for tumor imaging and combined photothermal and chemo-therapy. Theranostics 3, 633–649.

Chen, Y., Lun, A.T., Smyth, G.K., 2016. From reads to genes to pathways: differential expression analysis of RNA-Seq experiments using Rsubread and the edgeR quasi-likelihood pipeline. F1000Research 5, 1438.

Chu, Z., Zhang, S., Zhang, B., Zhang, C., Fang, C.Y., Rehor, I., Cigler, P., Chang, H.C., Lin, G., Liu, R., Li, Q., 2014. Unambiguous observation of shape effects on cellular fate of nanoparticles. Sci. Rep. 4, 4495.

Dam, D.H., Lee, J.H., Sisco, P.N., Co, D.T., Zhang, M., Wasielewski, M.R., Odom, T.W., 2012. Direct observation of nanoparticle-cancer cell nucleus interactions. ACS Nano 6, 3318–3326.

Ding, Y., Weindl, P., Lenz, A.-G., Mayer, P., Krebs, T., Schmid, O., 2020. Quartz crystal microbalances (QCM) are suitable for real-time dosimetry in nanotoxicological studies using VITROCELL®Cloud cell exposure systems. Part. Fibre Toxicol. 17, 44.

Dreaden, E.C., Austin, L.A., Mackey, M.A., El-Sayed, M.A., 2012. Size matters: gold nanoparticles in targeted cancer drug delivery. Ther. Deliv. 3, 457–478.

Falahati, M., Attar, F., Sharifi, M., Saboury, A.A., Salihi, A., Aziz, F.M., Kostova, I., Burda, C., Priecel, P., Lopez-Sanchez, J.A., Laurent, S., Hooshmand, N., El-Sayed, M. A., 2020. Gold nanomaterials as key suppliers in biological and chemical sensing, catalysis, and medicine. Biochim. Biophys. Acta (BBA) Gen. Subj. 1864, 129435.

Fan, Y.-N., Zhao, G., Zhang, Y., Ye, Q.-N., Sun, Y.-Q., Shen, S., Liu, Y., Xu, C.-F., Wang, J., 2023. Progress in nanoparticle-based regulation of immune cells. Med. Rev. 3, 152–179.

Favi, P.M., Gao, M., Johana Sepúlveda Arango, L., Ospina, S.P., Morales, M., Pavon, J.J., Webster, T.J., 2015. Shape and surface effects on the cytotoxicity of nanoparticles: Gold nanospheres versus gold nanostars. J. Biomed. Mater. Res. A 103, 3449–3462.

Fizeşan, I., Cambier, S., Moschini, E., Chary, A., Nelissen, I., Ziebel, J., Audinot, J.-N., Wirtz, T., Kruszewski, M., Pop, A., Kiss, B., Serchi, T., Loghin, F., Gutleb, A.C., 2019. In vitro exposure of a 3D-tetraculture representative for the alveolar barrier at the air-liquid interface to silver particles and nanowires. Part. Fibre Toxicol. 16, 14.

Forest, V., Leclerc, L., Hochepied, J.F., Trouvé, A., Sarry, G., Pourchez, J., 2017. Impact of cerium oxide nanoparticles shape on their in vitro cellular toxicity. Toxicol. Vitr. 38, 136–141.

Gharib, M., Khalaf, M., Afroz, S., Feliu, N., Parak, W.J., Chakraborty, I., 2019. Sustainable synthesis and improved colloidal stability of popcorn-shaped gold nanoparticles. ACS Sustain. Chem. Eng. 7, 9834–9841.

Gupta, R., Badhe, Y., Mitragotri, S., Rai, B., 2020. Permeation of nanoparticles across the intestinal lipid membrane: dependence on shape and surface chemistry studied through molecular simulations. Nanoscale 12, 6318–6333.

Hidalgo, A., Cruz, A., Pérez-Gil, J., 2015. Barrier or carrier? Pulmonary surfactant and drug delivery. Eur. J. Pharm. Biopharm. 95, 117–127.

Hühn, J., Carrillo-Carrion, C., Soliman, M.G., Pfeiffer, C., Valdeperez, D., Masood, A., Chakraborty, I., Zhu, L., Gallego, M., Yue, Z., Carril, M., Feliu, N., Escudero, A., Alkilany, A.M., Pelaz, B., del Pino, P., Parak, W.J., 2017. Selected standard protocols for the synthesis, phase transfer, and characterization of inorganic colloidal nanoparticles. Chem. Mater. 29, 399–461.

Jaber, N., Billet, S., 2023. How to use an in vitro approach to characterize the toxicity of airborne compounds. Toxicol. Vitr. 94, 105718.

Kim, S., Ryu, D.Y., 2013. Silver nanoparticle-induced oxidative stress, genotoxicity and apoptosis in cultured cells and animal tissues. J. Appl. Toxicol. 33, 78–89.

Klein, S.G., Serchi, T., Hoffmann, L., Blömeke, B., Gutleb, A.C., 2013. An improved 3D tetraculture system mimicking the cellular organisation at the alveolar barrier to study the potential toxic effects of particles on the lung. Part. Fibre Toxicol. 10, 31.

Klein, S.G., Cambier, S., Hennen, J., Legay, S., Serchi, T., Nelissen, I., Chary, A., Moschini, E., Krein, A., Blömeke, B., Gutleb, A.C., 2017. Endothelial responses of the alveolar barrier in vitro in a dose-controlled exposure to diesel exhaust particulate matter. Part. Fibre Toxicol. 14, 7.

Kodiha, M., Wang, Y.M., Hutter, E., Maysinger, D., Stochaj, U., 2015. Off to the organelles - killing cancer cells with targeted gold nanoparticles. Theranostics 5, 357–370.

Lacroix, G., Koch, W., Ritter, D., Gutleb, A.C., Larsen, S.T., Loret, T., Zanetti, F., Constant, S., Chortarea, S., Rothen-Rutishauser, B., Hiemstra, P.S., Frejafon, E., Hubert, P., Gribaldo, L., Kearns, P., Aublant, J.M., Diabaté, S., Weiss, C., de Groot, A., Kooter, I., 2018. Air-liquid interface in vitro models for respiratory toxicology research: consensus workshop and recommendations. Appl. Vitr. Toxicol. 4, 91–106.

Lamas, B., Martins Breyner, N., Houdeau, E., 2020. Impacts of foodborne inorganic nanoparticles on the gut microbiota-immune axis: potential consequences for host health. Part. Fibre Toxicol. 17, 19.

Lazaridis, M., 2023. Modelling approaches to particle deposition and clearance in the human respiratory tract. Air Qual. Atmos. Health 16, 1989–2002.

Lieber, M., Smith, B., Szakal, A., Nelson-Rees, W., Todaro, G., 1976. A continuous tumor-cell line from a human lung carcinoma with properties of type II alveolar epithelial cells. Int. J. Cancer 17, 62–70.

Marescotti, D., Serchi, T., Luettich, K., Xiang, Y., Moschini, E., Talikka, M., Martin, F., Baumer, K., Dulize, R., Peric, D., Bornand, D., Guedj, E., Sewer, A., Cambier, S., Contal, S., Chary, A., Gutleb, A.C., Frentzel, S., Ivanov, N.V., Peitsch, M.C., Hoeng, J., 2019. How complex should an in vitro model be? Evaluation of complex 3D alveolar model with transcriptomic data and computational biological network models. Altex 36, 388–402.

Müller, L., Gasser, M., Raemy, D.O., Herzog, F., Brandenberger, C., Schmid, O., Gehr, P., Rothen-Rutishauser, B., Clift, M.J.D., 2011. Realistic exposure methods for investigating the interaction of nanoparticles with the lung at the air-liquid interface in vitro. Insciences J. 1, 30–64.

Murugan, K., Choonara, Y.E., Kumar, P., Bijukumar, D., du Toit, L.C., Pillay, V., 2015. Parameters and characteristics governing cellular internalization and trans-barrier trafficking of nanostructures. Int. J. Nanomed. 10, 2191–2206.

Nahvi, I., Nahvi, I., Rehman, S., 2022. Nanotechnology and multidrug resistance. In: Hameed, S., Rehman, S. (Eds.), Nanotechnology for Infectious Diseases. Springer Singapore, Singapore, pp. 305–320.

Niikura, K., Matsunaga, T., Suzuki, T., Kobayashi, S., Yamaguchi, H., Orba, Y., Kawaguchi, A., Hasegawa, H., Kajino, K., Ninomiya, T., Ijiro, K., Sawa, H., 2013. Gold nanoparticles as a vaccine platform: influence of size and shape on immunological responses in vitro and in vivo. ACS Nano 7, 3926–3938.

Oberdörster, G., Oberdörster, E., Oberdörster, J., 2005. Nanotoxicology: an emerging discipline evolving from studies of ultrafine particles. Environ. Health Perspect. 113, 823–839.

Ortiz-Castillo, J.E., Gallo-Villanueva, R.C., Madou, M.J., Perez-Gonzalez, V.H., 2020. Anisotropic gold nanoparticles: a survey of recent synthetic methodologies. Coord. Chem. Rev. 425, 213489.

Riss, T., Niles, A., Moravec, R., Karassina, N., Vidugiriene, J., Markossian, S., Grossman, A., Brimacombe, K., Arkin, M., Auld, D., Austin, C., Baell, J., Chung, T.D. Y., Coussens, N.P., Dahlin, J.L., Devanarayan, V., Foley, T.L., Glicksman, M., Gorshkov, K., Haas, J.V., Hall, M.D., Hoare, S., Inglese, J., Iversen, P.W., Kales, S.C., Lal-Nag, M., Li, Z., McGee, J., McManus, O., Riss, T., Saradjian, P., Sittampalam, G. S., Tarselli, M., Trask, O.J., Jr., Wang, Weidner, Y., Wildey, J.R., Wilson, M.J., Xia, K., Xu, X., M. (Eds.), 2004. Cytotoxicity Assays: In Vitro Methods to Measure Dead Cells. Assay Guidance Manual. Eli Lilly & Company and the National Center for Advancing Translational Sciences, Bethesda (MD).

Romero, V.H., Kereselidze, Z., Egido, W., Michaelides, E.A., Santamaria, F., Peralta, X.G., 2014. Nanoparticle assisted photothermal deformation of individual neuronal organelles and cells. Biomed. Opt. Express 5, 4002–4012.

Rothen-Rutishauser, B.M., Kiama, S.G., Gehr, P., 2005. A three-dimensional cellular model of the human respiratory tract to study the interaction with particles. Am. J. Respir. Cell. Mol. Biol. 32, 281–289.

Russell, W.M.S., Burch, R.L., 1959. The Principles of Humane Experimental Technique. Methuen.

Schürch, D., Vanhecke, D., Clift, M.J., Raemy, D., de Aberasturi, D.J., Parak, W.J., Gehr, P., Petri-Fink, A., Rothen-Rutishauser, B., 2014. Modeling nanoparticle-alveolar epithelial cell interactions under breathing conditions using captive bubble surfactometry. Langmuir 30, 4924–4932.

Secondo, L.E., Liu, N.J., Lewinski, N.A., 2017. Methodological considerations when conducting in vitro, air-liquid interface exposures to engineered nanoparticle aerosols. Crit. Rev. Toxicol. 47, 225–262.

Silva, S., Bicker, J., Falcão, A., Fortuna, A., 2023. Air-liquid interface (ALI) impact on different respiratory cell cultures. Eur. J. Pharm. Biopharm. 184, 62–82.

Soliman, M.G., Pelaz, B., Parak, W.J., del Pino, P., 2015. Phase transfer and polymer coating methods toward improving the stability of metallic nanoparticles for biological applications. Chem. Mater. 27, 990–997.

de Souza Carvalho, C., Daum, N., Lehr, C.M., 2014a. Carrier interactions with the biological barriers of the lung: advanced in vitro models and challenges for pulmonary drug delivery. Adv. Drug Deliv. Rev. 75, 129–140.

de Souza Carvalho, C., Daum, N., Lehr, C.M., 2014b. Carrier interactions with the biological barriers of the lung: advanced in vitro models and challenges for pulmonary drug delivery. Adv. Drug Deliv. Rev. 75, 129–140.

St. Laurent, G., Shtokalo, D., Tackett, M.R., Yang, Z., Vyatkin, Y., Milos, P.M., Seilheimer, B., McCaffrey, T.A., Kapranov, P., 2013. On the importance of small changes in RNA expression. Methods 63, 18–24.

Suggs, J.E., Madden, M.C., Friedman, M., Edgell, C.J., 1986. Prostacyclin expression by a continuous human cell line derived from vascular endothelium. Blood 68, 825–829.

Talamini, L., Violatto, M.B., Cai, Q., Monopoli, M.P., Kantner, K., Krpetić, Ž., Perez-Potti, A., Cookman, J., Garry, D., Silveira, C.P., Boselli, L., Pelaz, B., Serchi, T., Cambier, S., Gutleb, A.C., Feliu, N., Yan, Y., Salmona, M., Parak, W.J., Dawson, K.A., Bigini, P., 2017. Influence of size and shape on the anatomical distribution of endotoxin-free gold nanoparticles. ACS Nano 11, 5519–5529.

Tsuchiya, S., Yamabe, M., Yamaguchi, Y., Kobayashi, Y., Konno, T., Tada, K., 1980. Establishment and characterization of a human acute monocytic leukemia cell line (THP-1). Int. J. Cancer 26, 171–176.

Vetten, M.A., Tlotleng, N., Tanner Rascher, D., Skepu, A., Keter, F.K., Boodhia, K., Koekemoer, L.A., Andraos, C., Tshikhudo, R., Gulumian, M., 2013. Label-free in vitro toxicity and uptake assessment of citrate stabilised gold nanoparticles in three cell lines. Part. Fibre Toxicol. 10, 50.

Vidgen, B., Yasseri, T., 2016. P-values: misunderstood and misused. Front. Phys. 4, 6.

Wirtz, T., De Castro, O., Audinot, J.N., Philipp, P., 2019. Imaging and analytics on the helium ion microscope. Annu. Rev. Anal. Chem. 12, 523–543.

Xie, X., Liao, J., Shao, X., Li, Q., Lin, Y., 2017. The effect of shape on cellular uptake of gold nanoparticles in the forms of stars, rods, and triangles. Sci. Rep. 7, 3827.

Xu, M., Soliman, M.G., Sun, X., Pelaz, B., Feliu, N., Parak, W.J., Liu, S., 2018. How entanglement of different physicochemical properties complicates the prediction of in vitro and in vivo interactions of gold nanoparticles. ACS Nano 12, 10104–10113.

Yacobi, N.R., Fazllolahi, F., Kim, Y.H., Sipos, A., Borok, Z., Kim, K.-J., Crandall, E.D., 2011. Nanomaterial interactions with and trafficking across the lung alveolar epithelial barrier: implications for health effects of air-pollution particles. Air Qual. Atmos. Health 4, 65–78.

Zhang, W., Taheri-Ledari, R., Ganjali, F., Mirmohammadi, S.S., Qazi, F.S., Saeidirad, M., KashtiAray, A., Zarei-Shokat, S., Tian, Y., Maleki, A., 2023. Effects of morphology and size of nanoscale drug carriers on cellular uptake and internalization process: a review. RSC Adv. 13, 80–114.